Cureus Journal of Engineering

Open Access Original Article

Influence of Co2+ Ions on Structural, Optical, and Magnetic Properties of Inverse Spinel Lithium Ferrite Nanoparticles

Received 12/14/2024
Review began 12/15/2024
Review ended 01/09/2025
Published 01/21/2025

DOI:
https://doi.org/10.7759/s44388-024-02854-9

Chetan S. Shinde [1, 2] , Nitin D. Sali [3] , Sachin K. Dhawale [1] , Vishakha N. Dhanwate [4] , Vivekanand Jawale [5]

1. Department of Applied Sciences and Humanities, Gharda Institute of Technology, Ratnagiri, IND 2. Engineering, Savitribai Phule Pune University, Pune, IND 3. Department of Electronic Science, Padmashri Vikhe Patil College of Arts, Science and Commerce, Ahmednagar, IND 4. Physics, Dr. D. Y. Patil Institute of Technology, Pune, IND 5. Chemistry, Modern College of Engineering, Pune, IND

Corresponding authors: Chetan S. Shinde, chetann.shinde@gmail.com, Nitin D. Sali, snitind7@gmail.com, Sachin K. Dhawale, skdhawale8215@gmail.com, Vishakha N. Dhanwate, itsmevishakha.vp@gmail.com, Vivekanand Jawale, vivekjawale25@gmail.com

Abstract

The Co-doped lithium ferrite ($LiCo_xFe_{1-x}O_4$) compound is made using a sol-gel auto-combustion process with metal nitrates and citric acid as fuel. The characterization techniques, including X-ray diffraction (XRD), field emission scanning electron microscopy (FE-SEM), transmission electron microscopy (TEM), Fourier transform infrared spectroscopy, UV-Vis spectroscopy, vibrating sample magnetometry, cyclic voltammetry, galvanostatic charge/discharge, and impedance, provide an idea about the Co^{2+} content on structural, microstructural, physical, and electrochemical properties. The crystallinity decreases to 13.72 nm as the Co^{2+} concentration increases, and when the Co^{2+} circumstances change, the magnetic characteristics improve as well and change from soft to hard magnetic material. FE-SEM micrographs clearly show defined grain development as the grain size decreased from 10 to 20 nm. The crystallite sizes observed in the XRD data are in good agreement with the TEM's estimate of the particle sizes, which range from 15 to 20 nm.

Categories: Advanced Materials, Nano Materials, Nanotechnology
Keywords: lithium ferrite, cobalt doping, sol-gel auto-combustion, crystallite size, vsm

Introduction

In the inverse spinel ferrite structure, half of the octahedral sites (B) are occupied by divalent metal ions (A^{2+}), while the other half are filled by trivalent ions (B^{3+}) [1]. The sol-gel auto-combustion method is a cost-effective technique for synthesizing ferrites, producing high-purity powders at low temperatures (Sol-gel auto combustion synthesis and characterizations of cobalt ferrite nanoparticles: Different fuels approach). It provides the ability to control crystallinity and phase purity, making it suitable for the development of advanced materials with customized properties [2]. Cobalt ferrite ($CoFe_2O_4$) is a magnetic compound recognized for its robust properties and stability. It features an inverse spinel structure, where Co^{2+} ions predominantly occupy octahedral sites, while Fe^{3+} ions are distributed across both tetrahedral and octahedral sites, contributing to its enhanced magnetic characteristics [3]. Cobalt ferrite is advantageous for various magnetic applications due to its low coercivity, high electrical resistivity, and excellent thermal stability, making it effective in minimizing eddy current losses [4,5]. Researchers are exploring the use of lithium ferrite in lithium-ion batteries and other energy storage devices due to its electrochemical characteristics. By introducing lithium in cobalt or altering the synthesis conditions, the properties of lithium ferrite can be adjusted to meet specific requirements [6].

Preeti Thakur et al. used the citrate precursor technique to produce cobalt-doped lithium ferrites. They verified the development of the α-phase using X-ray diffraction (XRD) and observed frequency shifts with different levels of cobalt doping using Fourier-transform infrared spectroscopy (FTIR) [7]. Using sol-gel combustion, M. K. Shobana synthesized lithium-doped cobalt ferrites with an average particle size of 15-20 nm. When lithium concentration increased, conductivity values somewhat dropped due to charge carrier mobility [8]. Cobalt-doped lithium ferrite nanoparticles were produced using the sol-gel process by Manish Srivastava et al. The evolution of distinct size and structural morphologies of the nanoparticles was shown to be significantly influenced by the fluctuation in pH during the production process [9]. Sameen Aslam and associates formed Li-NiCo ferrites by doping with neodymium (Nd) and praseodymium (Pr) using the micro-emulsion process. It has been approximated that Pr^{3+} and Nd^{3+} concentrations affect the magnetic structure and characteristics of lithium ferrite [10]. S. Malathi et al. developed lithium ferrite and lithium vanadium ferrite using a sol-gel method. It was reported that the average particle size of lithium ferrite is 22 nm, while vanadium-doped lithium ferrite has an average particle size of 29 nm [11].

The study aims to explore the impact of Cobalt doping on lithium ferrite for potential supercapacitor

applications. Using a cost-effective sol-gel auto-combustion method, Cobalt doping lithium ferrite was synthesized. The research indicates that doping lithium enhances the properties of cobalt ferrite, which holds promise for energy storage applications and future supercapacitors.

Materials And Methods

Sol-gel auto-combustion was used to synthesize the $LiCo_xFe_{2-x}O_4$ ferrite with varying x values, i.e., 0.0, 0.025, 0.050, and 0.075, as shown in Figure *1*. Ferric nitrate nonahydrate ($Fe(NO_3)_3{\cdot}9H_2O$), lithium nitrate hexahydrate ($LiNO_3{\bullet}6H_2O$), citric acid monohydrate ($C_6H_8O_7{\cdot}H_2O$), and cobalt (II) nitrate hexahydrate ($Co(NO_3)_2{\bullet}6H_2O$) are produced by Merck Chemical Company in India. High-purity AR grades of these chemicals were used as the starting materials. Citric acid and nitrates were maintained at a stoichiometric ratio of 1:3. Each nitrate and citric acid were separately dissolved in double-distilled water to produce clear aqueous solutions. These solutions were then combined and stirred continuously to achieve a homogeneous mixture. Ammonium hydroxide (30%) solution was added gradually to adjust the pH of the mixture to 7. The mixture was then stirred and heated gradually to 100 °C. Constant heating led to the formation of a thick gel, which solidified as all water molecules evaporated. The dry gel self-ignited, producing fine ash. The ash was then ground in a mortar to create a uniform powder. After annealing at 500 °C, the finished powder samples were used for further characterization.

FIGURE 1: Experimental detail of synthesis of LiCoxFe2-xO4 where x: 0.0, 0.025, 0.050, and 0.075

Characterizations

XRD examination is used to determine the structural properties of the produced $LiCo_xFe_{2-x}O_4$. A scanning electron microscopy (SEM) is used for structural analysis, and an energy-dispersive X-ray analysis (EDAX), which is connected to the SEM, is used for elemental analysis. Transmission electron microscopy (TEM) was used to analyze the size and shape of the nanoparticles. FTIR was used to determine the chemical composition and confirm the results. UV-Vis absorption spectroscopy was used to investigate the optical characteristics. Using a maximum applied field of 17,500 Oe at room temperature, the hysteresis loop, saturation magnetization, and coercivity of the nanocomposites were accurately measured with a

vibrating sample magnetometer (VSM) [12].

Results

X-ray diffraction

Figure 2 displays the XRD patterns for $LiCo_xFe_{2-x}O_4$ at different ($0.0 \leqslant x \leqslant 0.075$). The pattern was recorded in the 2θ range of 20 °-80 ° using Cu-Kα radiation (λ = 1.54182 Å). All the diffraction peaks could be attributed to reflections from the planes (220), (311), (222), (400), (422), (511), (440), and (440). These reflections could all be indexed to a face-centered cubic. Indexed patterns were compared to those in the databases JCPDS 22-1086 [13] and 41-0971 [14] for phase identification [15]. The XRD pattern's lack of extra peaks suggests that the $LiCo_xFe_{2-x}O_4$ is single-phase and free of impurity phases.

Crystallite size 'D', lattice constant 'a', X-Ray density 'dx', dislocation density 'ρD', and microstrain 'ε' were calculated using Equations (1) to (5) [16,17];

$$D = \frac{0.9\lambda}{\beta cos\theta} \text{.....(1)}$$

$$a = d\sqrt{h^2 + k^2 + l^2} \text{..... (2)}$$

$$d_x = \frac{8M}{Na^3} \text{..... (3)}$$

$$\varrho_D = \frac{1}{D * D} \text{..... (4)}$$

$$\varepsilon = \frac{\beta cos\theta}{4} \text{..... (5)}$$

where λ is the wavelength of the Cu-Kα radiation, β is the full breadth of the half maximum of Bragg's angle θ, (hkl) is the XRD reflection peak index, N denotes Avogadro's number, M is sample molecular weight, and d is the interplanar separation.

The lattice parameters varied from 9.244 to 9.188 Å, whereas the average crystallite size was determined to be between 18 and 13 nm. During the synthesis, Li+ ions replace Co^{2+} ions. This replacement modifies the lattice constant by shifting the positions of the cobalt ions inside the crystal lattice, which in turn modifies the arrangement of the atoms [18]. It is the degree of ion substitution and the resulting lattice distortions caused by the variations in ionic radii between Co and Li ions that will define the exact influence on the diameters of the crystallites. The structure of $LiCo_xFe_{2-x}O_4$ allows for the presence of Co^{2+} and Fe^{3+} ions in both tetrahedral and octahedral locations [19]. Moving to octahedral locations causes the lithium ions to arrange more compactly, resulting in smaller crystallites. In contrast, migration to tetrahedral positions produces larger crystallites. The X-ray density (dx) [20] increases from 3.044 to 3.671 gm/cc, almost linearly with the amount of Co^{2+} doping [21]. The microstrain and dislocation density [22] are 0.00207 to 0.00273 % and 0.0145 to 0.0186 line/m^2, respectively. This occurs when a larger mass of Co^{2+} ions replaces the Fe^{3+} ions on the octahedral sites. Furthermore, microstrain values increase with Co^{2+} concentration, which can be attributed to grain size's impact on the material's overall stress [23]. Here, structural parameters are given in Table 1.

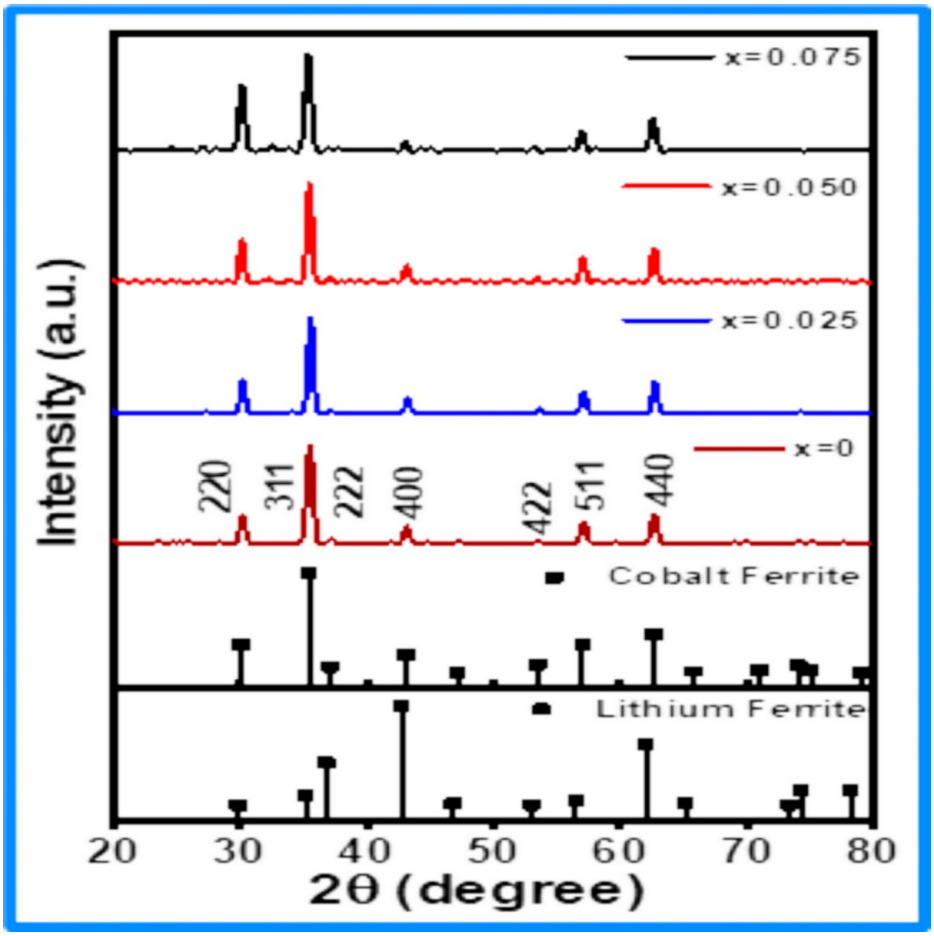

FIGURE 2: XRD analysis of LiCoxFe2-xO4 where x: 0.0, 0.025, 0.050, and 0.075

XRD, X-ray diffraction

Field emission scanning electron microscopy (FE-SEM)

With the aid of Windows®-based Smart SEM control software, FE-SEM investigation of a sample of $LiCo_xFe_{2-x}O_4$ at x = 0.075 was carried out using the Carl Zeiss Model Supra 55 (Germany) with an installation of Windows®-based Smart FE-SEM control software. Figure *3A* displays the $LiCo_xFe_{2-x}O_4$ nanoparticle's FE-SEM micrographs, which in some regions exhibit nearly spherical-shaped particles and in others, a structure like a flower. Figure *3C* displays the histogram of the acquired FE-SEM image. It displays that the material's mean grain size is 287.55 nm. Figure *3B* displays the EDAX spectrum of the sample under study, allowing for the identification and characterization of the constituent elements and their relative quantities. It shows that the primary elements present are iron, lithium, cobalt, and oxygen; no indication of contamination from other elements is found. The peaks in the EDAX spectrum properly reflect the true composition of the item under investigation. Table *2* provides an analytical analysis of the EDAX spectra and shows the relative proportions of the components. Furthermore, EDAX mapping is provided for the composition of the produced $LiCo_xFe_{2-x}O_4$ with x = 0.075, as seen in Figure *3D*-G. It seems from the image that each component is distributed equally. Fe, O, Co, and Li are represented by the colors brown, red, blue, and yellow, in that order.

Name of samples	Crystallite size (nm)	Lattice constant (Å)	X-ray density gm/cc	Dislocation density line/nm^2	Microstrain %
$LiCo_xFe_{2-x}O_4$ S_1	15.45	9.244	3.044	0.00145	0.0024
$LiCo_xFe_{2-x}O_4$ S_2	18	9.221	3.274	0.00308	0.0020
$LiCo_xFe_{2-x}O_4$ S_3	17.7	9.246	3.424	0.00319	0.0021
$LiCo_xFe_{2-x}O_4$ S_4	13.72	9.188	3.671	0.00531	0.0027

TABLE 1: Values of crystallite size, lattice constant, X-ray density, dislocation density, and microstrain of LiCoxFe2-xO4

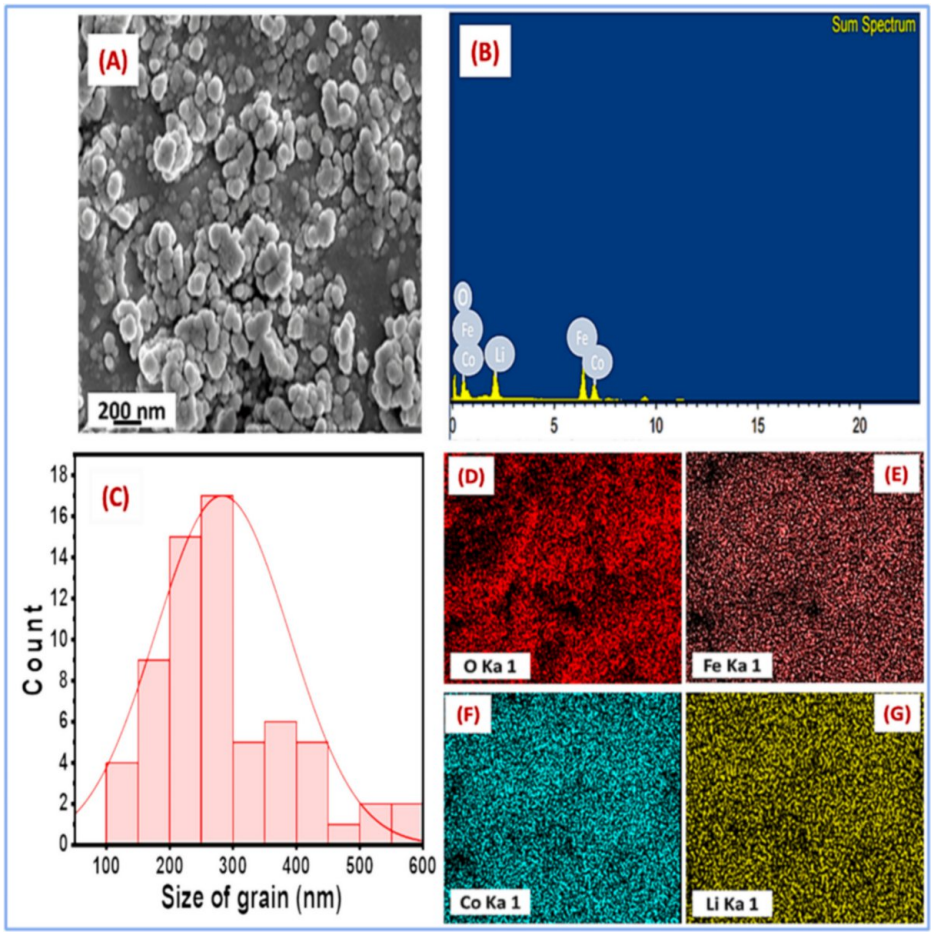

FIGURE 3: (A) FE-SEM image, (B) EDAX analysis, (C) histogram from FE-SEM image, and (D-G) mapping of O, Fe, Co, and Li of LiCoxFe2-xO4 at x = 0.075

FE-SEM, field emission scanning electron microscopy; EDAX, energy-dispersive X-ray analysis

Elements	Weight %	Atomic weight %
Li K	30.01	23
O K	14.52	40.37
Co K	26.76	15.74
Fe K	28.71	20.89
	100.00	

TABLE 2: EDAX elemental analysis of LiCoxFe2-xO4 (x = 0.075)

EDAX, energy-dispersive X-ray analysis

High-resolution transmission electron microscopy (HR-TEM)

The HR-TEM image of $LiCo_xFe_{2-x}O_4$ at x = 0.075 is shown in Figure *4A*. It showed that there was some little agglomeration in the sample and that surface energy during preparation gave the sample a roughly spherical form. Figure *4B* provides evidence that the predicted particle size ranges between 16 and 21 nm, which closely matches the crystallite sizes given in the XRD data. With the use of an HR-TEM, the selected area electron diffraction pattern of $LiCo_xFe_{2-x}O_4$ at x = 0.075 is displayed in Figure *4C*, displaying a superimposed bright spot that denotes the polycrystalline nature of the nanoparticles. This result confirms the particle dispersion seen in the XRD study.

UV-Vis spectra

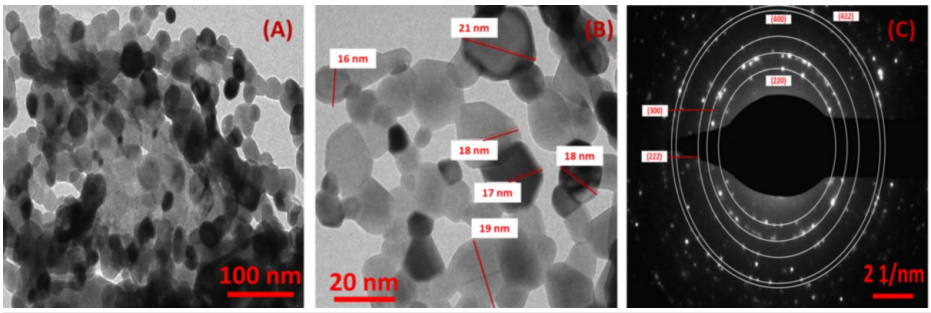

FIGURE 4: (A and B) HR-TEM image and (C) SAED pattern of LiCoxFe2-xO4 at x = 0.075

HR-TEM, high-resolution transmission electron microscopy; SAED, selected area electron diffraction

Figure *5A* displays the wavelength-dependent UV-Vis absorption spectra of $LiCo_xFe_{2-x}O_4$ (x = 0 to 0.075) nanoparticles synthesized via sol-gel auto-combustion in the 200-800 nm wavelength range. The band gap energy was calculated using the direct formula 6 [24].

$$E_g = \frac{1239}{\lambda} \text{.....(6)}$$

where λ denotes the wavelength and Eg stands for the band gap energy [25]. The band gap energy obtained from the equation shifts from 2.07 to 1.74 eV as the amount of Co^{2+} increases, as shown in Figure *5* and Table *3*. These values show that the obtained material is a semiconductor material. Distortions in the lattice structure can result from the presence of lithium ions because the ionic radii of Li^+ and Co^{2+} or Fe^{3+} differ, which may be impacted by these instabilities, which may then have an impact on the energy levels of the electronic state and narrow the band gap [26]. The distribution of cations between the tetrahedral (A) and octahedral (B) sites can be changed by lithium, which has an impact on the band structure as a whole and lowers the band gap.

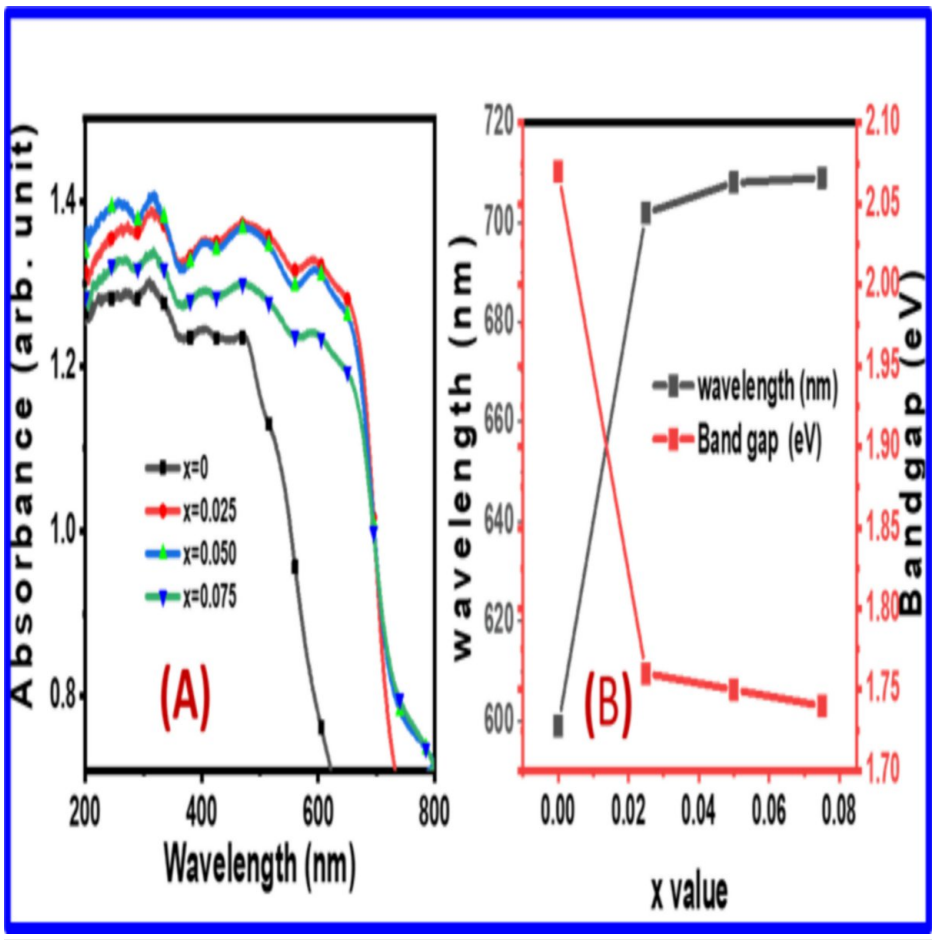

FIGURE 5: (A) UV-Vis absorption spectra and (B) variation of band gap with various concentrations of LiCoxFe2-xO4 where x: 0.0, 0.025, 0.050, and 0.075

Name of samples	Object wavelength (nm)	Band gap (eV)
$LiCo_xFe_{2-x}O_4$ S_1	599	2.07
$LiCo_xFe_{2-x}O_4$ S_2	702	1.76
$LiCo_xFe_{2-x}O_4$ S_3	708	1.75
$LiCo_xFe_{2-x}O_4$ S_4	709	1.74

TABLE 3: The variation of band gap for different concentrations of LiCoxFe2-xO4 where x: 0.0, 0.025, 0.050, and 0.075

Fourier transform infrared (FTIR) spectra

FTIR spectra, which were obtained in the 400-2000 cm^{-1} wave number range, were used to analyze the structural characteristics of a $LiCo_xFe_{2-x}O_4$ and are shown in Figure *6A*. Two well-defined peaks can be seen in the $LiCo_xFe_{2-x}O_4$ FTIR spectrum. Tetrahedral complexes (v1) are responsible for the peak at roughly 560-550 cm^{-1}, while the high peak at 400-460 cm^{-1} is caused by the stretching vibrations of octahedral site complexes (v2), i.e. metal cation and oxygen [27], given in Table *4*. The difference in bond length between the octahedral and tetrahedral positions also affects the band position shift. Force constants at octahedral site Ko, tetrahedral site Kt, and Debye temperatures θE [28] are calculated using Equations (7) to (9) [29].

$$k_t = 4\pi^2 c^2 \nu_1^2 \mu \text{.....(7)}$$

$$k_o = 4\pi^2 c^2 \nu_2^2 \mu \text{.....(8)}$$

$$\theta_E = \frac{hc\nu_{av}}{K\beta} \text{.....(9)}$$

In the $LiCo_xFe_{2-x}O_4$, the average band wavenumber is vav, c is the speed of light (2.99 × 1010 cm/s), and μ is the decreased mass of the ions (2.061 × 10^{-23} g) for Fe^{3+} and O^{2-}. In this case, Kβ stands for the Boltzmann constant, 1.380649 × 10^{-23} J/K, and h is the Planck constant (h = 6.626 × 10^{-34} J•s).

The bond length increases when the radius of Li^+ ions is larger than that of Co^{2+} ions, resulting in a decrease in the force constant for both sites, leading to a reduction in electrostatic energy and a lower wavenumber. The FTIR data confirm that Li^+ ions are stabilized in the Oh crystal field as expected, but they occupy Td sites [30]. Analyzing the differences in force constants with Co^{2+} for each $LiCo_xFe_{2-x}O_4$ sample necessitates a critical examination of the Fe^{3+}-O^{2-} band at tetrahedral and octahedral sites. It is observed that the force constants Ft and Fo increase as the concentration of Co^{2+} rises due to the variation in cation-oxygen bond length.

The Debye temperatures (θE) of $LiCo_xFe_{2-x}O_4$ vary with increasing Co^{2+} concentration, as shown in Figure *6B* and Table *4*. The maximum value of θE is 687.6278 K at x = 0.075. Understanding the conduction mechanism of these ferrites is crucial, and these data point to an enhancement in the lattice vibrations. This suggests that the conduction observed in these samples is most likely the result of n-type electrons. The increase in θE is mainly caused by a decrease in the wavenumber of the peak, which is caused by the vibration of the Me-O bond in the tetrahedral site.

Sr. No.	Material	Synthesis method	Crystallite size (nm)	References
1	Vanadium-doped lithium ferrite	Sol-gel	22	[11]
2	Aluminium-substituted lithium nano ferrite	Citrate gel method	27	[31]
3	Cr-doped lithium ferrite	Sol-gel	44	[32]
6	Present work	Sol-gel auto-combustion	13	This work

TABLE 4: Comparison of present work with other ferrite material

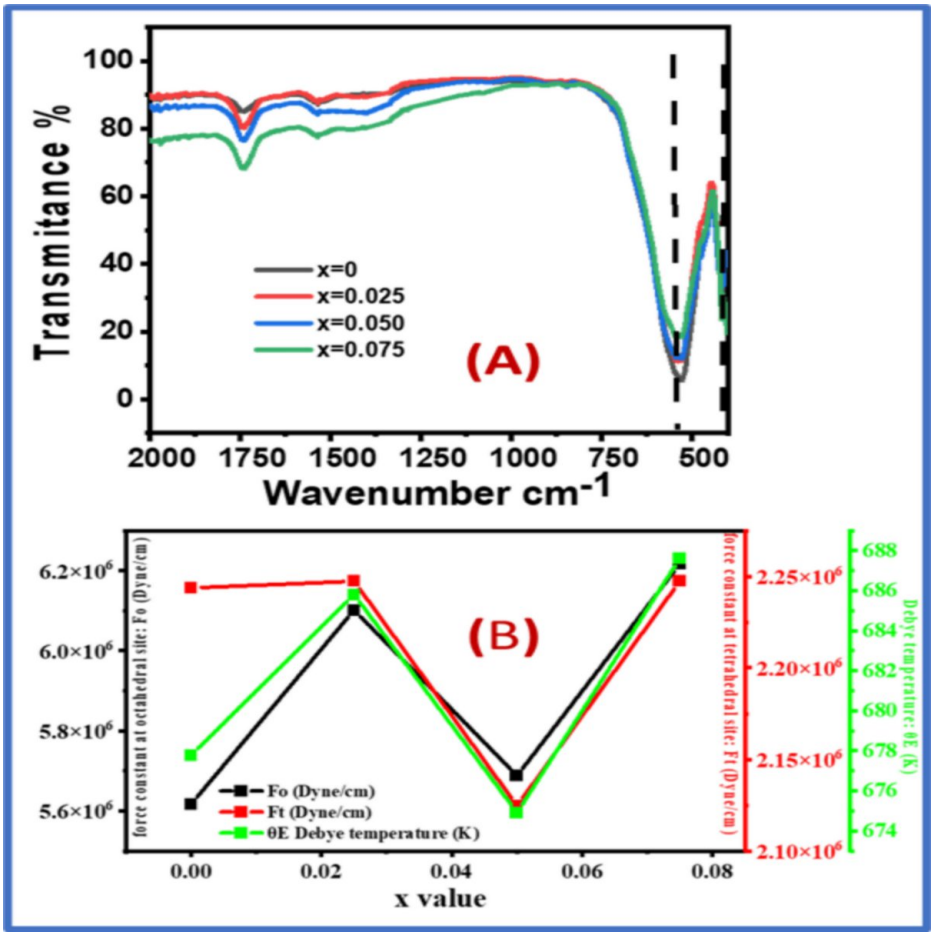

FIGURE 6: (A) FTIR spectra of LiCoxFe2-xO4 where x: 0.0, 0.025, 0.050, and 0.075 and (B) variations in the force constant at the octahedral site (Fo), tetrahedral site (Ft), and Debye temperature θE of LiCoxFe2-xO4 where x: 0.0, 0.025, 0.050, and 0.075

FTIR, Fourier transform infrared spectroscopy

Name of samples	v_2 cm^{-1}	v_1 cm^{-1}	F_o (dyne/cm)	F_t (dyne/cm)	Debye temperature (K)
$LiCo_xFe_{2-x}O_4$ S_1	418.38	526.26	5616646.47	2243671.68	677.783
$LiCo_xFe_{2-x}O_4$ S_2	418.55	537.27	6101631.96	2247320.58	685.805
$LiCo_xFe_{2-x}O_4$ S_3	412.72	527.92	5687849.61	2124700.42	674.913
$LiCo_xFe_{2-x}O_4$ S_4	418.56	539.8	6217376.46	2247535.36	687.627

TABLE 5: Change in force constant of LiCoxFe2-xO4 where x: 0.0, 0.025, 0.050, and 0.075

Vibrating-sample magnetometry (VSM)

Figure 7 displays the results of the magnetic analysis performed on the $LiCo_xFe_{2-x}O_4$ samples. The saturation magnetization (Ms), remanence (Mr), and coercivity (Hc) of Cobalt ferrite on Li^+ doping are described here. These results are attributed to Neel's two sublattice models, in which the ions occupying these sites have their magnetic moments organized antiparallelly due to exchange energy [33]. The prepared materials convert soft to hard magnetic material as Co^{2+} ions increase. The distribution of Fe^{3+}

and Li^+ ions in the material's A and B sites affects its magnetic behavior. The net magnetic moment is determined by the Li^+ ions, and the total magnetization is influenced by the higher concentration of ions at the B site. The presence of non-magnetic Co^{2+} ions leads to interesting magnetic behavior, causing the magnetization to decrease as Fe^{3+} ions shift from A to B sites due to Co^{2+}'s preference for A sites, thereby increasing magnetization. With an increase in Co^{2+} value, the coercivity (Hc) value rises from 20.89 Oe to 109.1111 Oe before progressively declining. These variations may result from variations in the grain and particle sizes of $LiCo_xFe_{2-x}O_4$. In $LiCo_xFe_{2-x}O_4$, magneto-crystalline anisotropy (K) [34] is calculated by Equation (10),

$$H_c = \frac{2K}{Ms} \quad \text{.....(10)}$$

The anisotropy (K) value increases at x = 0.025 and decreases as the concentration of Co^{2+} increases (Table 5). This increase in K is associated with a rise in coercive force, which varies with the Co^{2+} concentration, suggesting that higher Co^{2+} concentrations tend to occupy ⊠-sites, leading to an increase in the K value. This has significant implications for creating novel materials with improved magnetic properties.

$$n\beta = \frac{Ms * MolecularWt}{5585} \quad \text{.....(11)}$$

The amount of Bohr magnetons [35] is calculated using Equation (11). The non-linear variation in nB implies that the magnetization of $LiCo_xFe_{2-x}O_4$ may be influenced by spin canting. The octahedral sites of $LiCo_xFe_{2-x}O_4$ exhibit a triangular spin configuration due to the replacement of Li^+. The degree of spin canting increases with Co^{2+} in lithium ferrite, demonstrating its effectiveness. When x = 0.025, the values of nB increase to 1.1357 and subsequently decrease. This research is significant as it shows how spin canting can control magnetization in similar materials and provides insights into magnetization in $LiCo_xFe_{2-x}O_4$. The squareness ratio (Mr/Ms) increases with more Co^{2+} ions, going from 0.7199 to 0.3861. When the squareness ratio (R) is less than 0.5 [36], ferrite materials have a multi-domain structure; when it is larger than 0.5, $LiCo_xFe_{2-x}O_4$ has a single-domain structure. The values of all magnetic parameters are given in the Table 6.

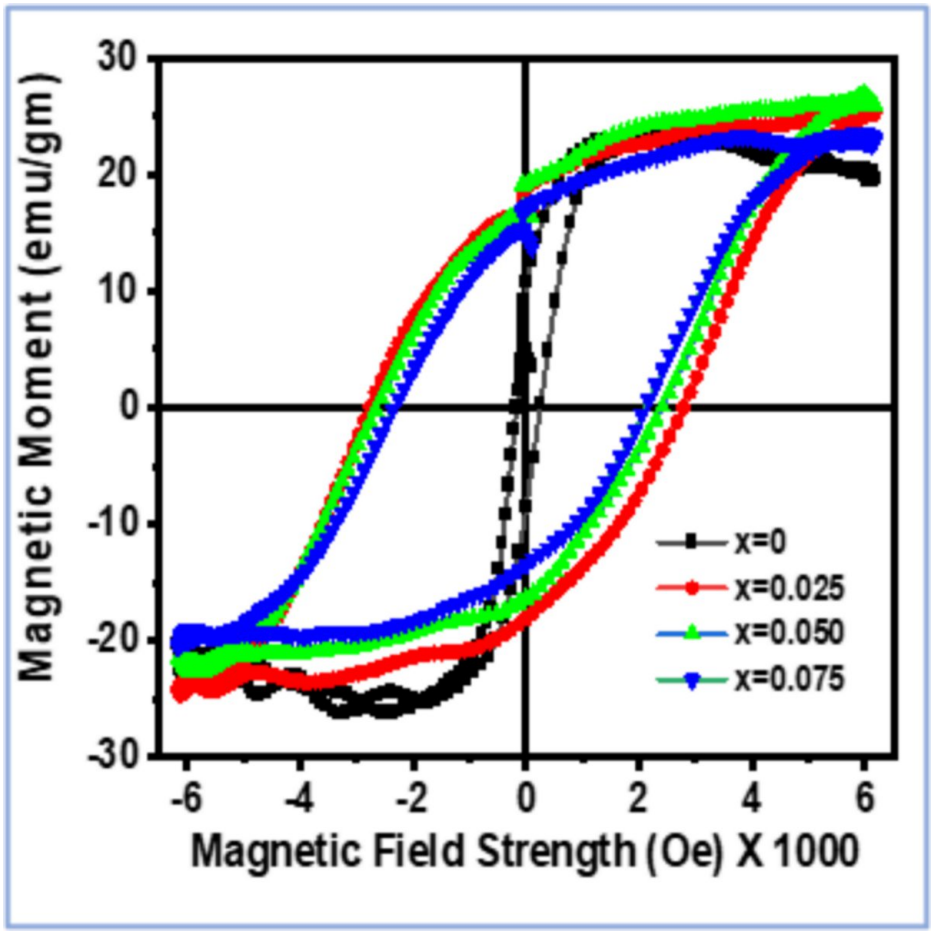

FIGURE 7: The magnetic behavior of of LiCoxFe2-xO4 where x: 0.0, 0.025, 0.050, and 0.075

Name of samples	Hc (Oe)	Mr (emu/gm)	Ms (emu/gm)	Anisotropy constant K	Bohr magneton (B)	Squareness ratio (Mr/Ms)
$LiCo_xFe_{2-x}O_4$ S_1	20.89	18.65	27.10	283.00	0.89	0.69
$LiCo_xFe_{2-x}O_4$ S_2	109.11	18.59	25.82	1408.85	1.14	0.72
$LiCo_xFe_{2-x}O_4$ S_3	63.89	9.63	24.94	796.59	0.91	0.39
$LiCo_xFe_{2-x}O_4$ S_4	37.44	16.39	24.27	454.31	0.93	0.68

TABLE 6: Change in magnetic parameters concerning of LiCoxFe2-xO4 where x: 0.0, 0.025, 0.050, and 0.075

Discussion

The findings of the present work consist of increasing cobalt content in lithium ferrite leading to a decrease in crystallite size. Cobalt ions (Co^{2+} and Co^{3+}) replace Fe^{3+} ions in the lattice. The ionic radius of Co^{2+}(0.74 Å) is slightly larger than that of Fe^{3+} (0.64 Å), and Co^{3+} (0.545 Å) is even smaller. This size mismatch causes lattice distortions, hindering crystallite growth and resulting in smaller particles. The strain from the size difference limits lattice expansion, while cobalt doping also introduces defects like vacancies and dislocations, further restricting crystallite growth (Figure *8*).

Cobalt's oxidation state influences crystallite size. Co^{2+} induces more strain than Co^{3+}, disrupting charge distribution and interactions with oxygen ions, which suppresses larger crystallite formation. Co^{2+} also introduces additional electron states near the conduction band, narrowing the band gap. This is due to

interactions between Co^{2+}-Fe^{3+} and Co^{3+}-Fe^{3+} and the hybridization of Co^{2+} and Fe^{3+} 3d orbitals, which creates intermediate energy levels. These effects lower the energy required for electron transitions and enhance electron delocalization, increasing conductivity.

In summary, cobalt doping reduces crystallite size and narrows the bandgap due to strain, defects, and charge transfer mechanisms that modify the electronic structure and improve conductivity.

The findings show the prepared material can be used in the supercapacitor in the future for supercapacitor application. The specific capacitance will be increased as cobalt is doped in the lithium ferrite.

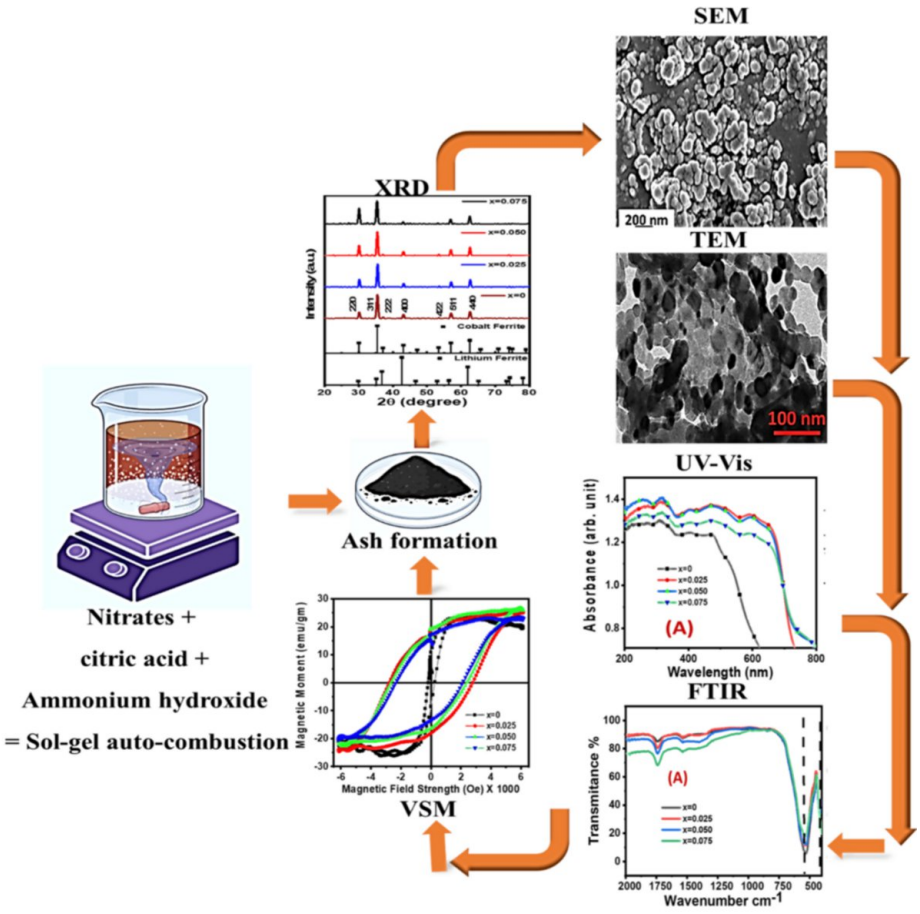

FIGURE 8: Discussion and graphical abstract of the present manuscript procedure and result

SEM, scanning electron microscopy; TEM, transmission electron microscopy; XRD, X-ray diffraction; VSM, vibrating sample magnetometry; FTIR, Fourier transform infrared spectroscopy

Conclusions

Lithium ferrites doped with cobalt ($LiCo_xFe_{2-x}O_4$), where x ranges from 0 to 0.075, were successfully synthesized using the sol-gel auto-combustion method. XRD analysis confirmed a single-phase cubic spinel structure, with crystallite sizes observed between 18 nm and 13.72 nm. As the concentration of Li^+ ions increased in the cobalt ferrite, the lattice parameters expanded from 9.221 to 9.187 Å, which was attributed to the substitution of smaller ions by larger ones. The Raman peaks in the range of 400-460 cm^{-1} corresponded to the stretching vibrations of metal cations and oxygen in octahedral sites, while the peak around 550-560 cm^{-1} was linked to tetrahedral site complexes. FE-SEM images revealed well-defined grain growth, with the grain size reducing from 10 to 20 nm. TEM analysis estimated particle sizes between 16 and 21 nm, which correlated closely with the crystallite sizes obtained from the XRD data. VSM analysis showed that as the lithium content increased, the material transitioned from a soft to a hard ferromagnetic state. Additionally, UV-Vis spectroscopy indicated a trend of increasing optical band gap energy with higher cobalt doping concentrations.

Additional Information

Author Contributions

All authors have reviewed the final version to be published and agreed to be accountable for all aspects of the work.

Concept and design: Chetan S. Shinde, Nitin D. Sali, Sachin K. Dhawale, Vishakha N. Dhanwate, Vivekanand Jawale

Acquisition, analysis, or interpretation of data: Chetan S. Shinde, Nitin D. Sali, Vivekanand Jawale

Drafting of the manuscript: Chetan S. Shinde, Nitin D. Sali, Vivekanand Jawale

Critical review of the manuscript for important intellectual content: Chetan S. Shinde, Nitin D. Sali, Sachin K. Dhawale, Vishakha N. Dhanwate, Vivekanand Jawale

Supervision: Chetan S. Shinde, Nitin D. Sali, Vivekanand Jawale

Disclosures

Human subjects: All authors have confirmed that this study did not involve human participants or tissue. **Animal subjects:** All authors have confirmed that this study did not involve animal subjects or tissue. **Conflicts of interest:** In compliance with the ICMJE uniform disclosure form, all authors declare the following: **Payment/services info:** All authors have declared that no financial support was received from any organization for the submitted work. **Financial relationships:** All authors have declared that they have no financial relationships at present or within the previous three years with any organizations that might have an interest in the submitted work. **Other relationships:** All authors have declared that there are no other relationships or activities that could appear to have influenced the submitted work.

References

1. Issa B, Obaidat IM, Albiss BA, Haik Y: Magnetic nanoparticles: surface effects and properties related to biomedicine applications. International Journal of Molecular Sciences. 2013, 14:21266-305. 10.3390/ijms141121266
2. Raut AV, Barkule RS, Shengule DR, Jadhav KM: Synthesis, structural investigation and magnetic properties of Zn2+ substituted cobalt ferrite nanoparticles prepared by the sol-gel auto-combustion technique. Journal of Magnetism and Magnetic Materials. 2014, 358-359:87-92. 10.1016/j.jmmm.2014.01.039
3. Silva JB, de Brito W, Mohallem NDS: Influence of heat treatment on cobalt ferrite ceramic powders. Materials Science and Engineering: B. 2004, 112:182-87. 10.1016/j.mseb.2004.05.029
4. Sharifianjazi F, Moradi M, Parvin N, et al.: Magnetic CoFe2O4 nanoparticles doped with metal ions: a review. Ceramics International. 2020, 46:18391-412. 10.1016/j.ceramint.2020.04.202
5. Pandit UV, Arbuj SS, Pandit Y, et al.: Solar light driven dye degradation using novel organo-inorganic (6, 13-pentacenequinone-TiO2) nanocomposite. The Royal Society of Chemistry. 2013, 5:10326-331.
6. Mubasher, Mumtaz M, Mehwish H, Ullah S, Ahmad Z: Nanohybrids of multi-walled carbon nanotubes and cobalt ferrite nanoparticles: high performance anode material for lithium-ion batteries. Carbon. 2021, 171:179-87. 10.1016/j.carbon.2020.08.080
7. Thakur P, Sharma P, Mattei JL, et al.: Influence of cobalt substitution on structural, optical, electrical and magnetic properties of nanosized lithium ferrite. Journal of Materials Science: Materials in Electronics. 2018, 29:16507-515. 10.1007/s10854-018-9744-2
8. Shobana MK: Electrical and structural studies of lithium doped cobalt ferrite. Journal of Physics and Chemistry of Solids. 2012, 73:1040-43. 10.1016/j.jpcs.2012.03.009
9. Srivastava M, Ojha AK, Chaubey S, Sharma PK, Pandey AC: Influence of pH on structural morphology and magnetic properties of ordered phase cobalt doped lithium ferrites nanoparticles synthesized by sol-gel method. Materials Science and Engineering: B. 2010, 175:14-21. 10.1016/j.mseb.2010.06.005
10. Aslam S, Muhammad SS, Gilani ZA, et al.: Structural, optical and magnetic elucidation of co-doping of Nd3+ and Pr3+ on lithium nanoferrite and its technological application. Results in Physics. 2019, 12:1334-39. 10.1016/j.rinp.2019.01.018
11. Malathi S, Sridhar B, Wayessa SG: A study of lithium ferrite and vanadium-doped lithium ferrite nanoparticles based on the structural, optical, and magnetic properties. Journal of Nanomaterials. 2023, 2023:10.1155/2023/6752950
12. Pandit S, Shaikh R, Pandit V: Synthesis of 5-unsubstituted -3,4-dihydropyridine 2-(1h)- ones using NBS as a catalyst under solvent free conditions. Rasayan Journal of Chemistry. 2009, 2:907-11.
13. Ateia EE, Ateia MA, Fayed MG, El-Hout SI, Mohamed SG, Arman MM: Synthesis of nanocubic lithium cobalt ferrite toward high-performance lithium-ion battery. Applied Physics A. 2022, 128:483. 10.1007/s00339-022-05622-w
14. Stein CR, Bezerra MTS, Holanda GHA, André-Filho J, Morais PC: Structural and magnetic properties of cobalt ferrite nanoparticles synthesized by co-precipitation at increasing temperatures. AIP Advances. 2018, 8:056303. 10.1063/1.5006321
15. Pandit VRU, Jadhav GKP, Jawale VMS, Dubepatil R, Gurao R, Late DJ: Synthesis and characterization of micro-/nano-aFe2O3 for photocatalytic dye degradation. RSC Advances. 2014, 14:29099-105 .
16. Chilwar RR, Somvanshi SB, Chavan AR, Kharat PB, Babrekar MK, Jadhav KM: Synthesis and characterization of

spray deposited lithium ferrite thin film. Applied Nanotechnology and Nanoscience. 2017, 73-76.
17. Yakob M, Hamdani U, Puji W, Putra RA: Characterization of microstructural and optical CoFe2O4/SiO2 ferrite nanocomposite for photodegradation of methylene blue. AIMS Materials Science. 2019, 6:45-51. 10.3934/matersci.2019.1.45
18. Krishna KR, Ravinder D, Kumar KV, Lincon CA: Synthesis, XRD & SEM studies of zinc substitution in nickel ferrites by citrate gel technique. World Journal of Condensed Matter Physics. 2012, 2:153-59. 10.4236/wjcmp.2012.23025
19. Zhang Z, Wenyue L, Rujia Z, et al.: Layer-stacked cobalt ferrite (CoFe2O4) mesoporous platelets for high-performance lithium ion battery anodes. Journal of Materials Chemistry A. 2015, 3:6990-97. 10.1039/c5ta00073d
20. Shyamaldas, Bououdina M, Manoharan C: Dependence of structure/morphology on electrical/magnetic properties of hydrothermally synthesised cobalt ferrite nanoparticles. Journal of Magnetism and Magnetic Materials. 2020, 493:165703. 10.1016/j.jmmm.2019.165703
21. Duthade GS, Joshi UD, Kodape MM, et al.: Synthesis, X-ray diffraction, physical, thermal behavior and chemical studies of Fe/Zn/Cu-NaX zeolite. Materials Today: Proceedings. 2022, 53:15-23.
22. Hankare PP, Sanadi KR, Pandav RS, Patil NM, Garadkar K, Mulla IS: Structural, electrical and magnetic properties of cadmium substituted copper ferrite by sol-gel method. Journal of Alloys and Compounds. 2012, 540:290-96. 10.1016/j.jallcom.2012.06.018
23. Kulkarni AB, Mathad SN: Synthesis and structural analysis of Co-Zn-Cd ferrite by Williamson-Hall and size-strain plot methods. International Journal of Self-Propagating High-Temperature Synthesis. 2018, 27:37-43. 10.3103/s106138621801003x
24. Chhattise PK, Saleh S, Pandit V, Arbuj S, Chabukswar V: Zno nanostructures: a heterogeneous catalyst for the synthesis of benzoxanthene and pyranopyrazole scaffolds via multicomponent reaction strategy. Materials Today: Proceedings. 2020, 1:2339-45. 10.1039/D0MA00403K
25. Bagade A, Nagwade P, Nagawad A, Thopate S, Pandit V, Pund S: Impact of Mg2+ substitution on structural, magnetic and optical properties of Cu-Cd ferrites. Materials Today: Proceedings. 2022, 53:144-52.
26. Latif Z, Rehman AU, Nasir A, Arshad MI, Marzouki R: Graphene nanoplatelets (GNPs): a source to bring change in the properties of Co-Ni-Gd-ferrite/GNP nanocomposites. RSC Advances. 2023, 13:34308-321. 10.1039/d3ra02080k
27. Yuliantika D, Ahmad T, Arif H, Sunaryono, Hidayat N, Soontaranon S: Exploring structural properties of cobalt ferrite nanoparticles from natural sand. IOP Conference Series: Materials Science and Engineering. 2019, 515:012047. 10.1088/1757-899x/515/1/012047
28. Harak C, Mardikar S, Gulavani V, et al.: Superior photoelectrochemical performance of Fe2O3/g-C3N4 heterostructure synthesized by chemical precipitation method. Materials Today: Proceedings. 2022, 53:134-38.
29. Ledneva AY, Ivanova MN, Poltarak PA, Yarovoy SS, Kolesov BA, Fedorov VE, Naumov NG: Systematic study of vibrational spectra of octahedral rhenium clusters {Re6S8-xBrx}Bry (x = 0, 1, 2, 3, 4) with mixed sulfur/bromine inner ligands. Symmetry. 2023, 15:1791. 10.3390/sym15091791
30. Channa N, Khalid M, Chandio AD, et al.: Structural, dielectric, impedance, and electric modulus properties of Cu2+-substituted CuxMn1-xFe2O4 spinel ferrites nanoparticles. Journal of Materials Science: Materials in Electronics. 2021, 32:2832-44. 10.1007/s10854-020-05036-5
31. Nayak DR, Gaffoor A, Aravind G, Ravinder D: Preparation and structural properties of aluminium substituted lithium nano ferrites by citrate-gel auto combustion method. IOSR Journal of Applied Physics. 2015, 7:43-49.
32. Srivastava M, Layek S, Singh J, et al.: Synthesis, magnetic and Mössbauer spectroscopic studies of Cr doped lithium ferrite nanoparticles. Journal of Alloys and Compounds. 2014, 591:174-80.
33. Zheng Z, Guo XZ, Zhong YJ, Hua WB, Shen CH, Chou SL, Yang XS: Host structural stabilization of Li1.232Mn0.615Ni0.154O2 through K-doping attempt: toward superior electrochemical performances. Electrochimica Acta. 2016, 188:336-43. 10.1016/j.electacta.2015.12.021
34. Andersen HL, Saura-Múzquiz M, Granados-Miralles C, Canévet E, Lock N, Christensen M: Crystalline and magnetic structure-property relationship in spinel ferrite nanoparticles. Nanoscale. 2018, 10:14902-914. 10.1039/c8nr01534a
35. Mitra A, Mohapatra J, Aslam M: Magnetic and electronic properties of anisotropic magnetite nanoparticles. Materials Research Express. 2024, 11:022002. 10.1088/2053-1591/ad2a84
36. Nath SK, Maria KH, Noor S, Sikder SS, Hoque SM, Hakim MA: Magnetic ordering in Ni-Cd ferrite. Journal of Magnetism and Magnetic Materials. 2012, 324:2116-20. 10.1016/j.jmmm.2012.02.023